RESEARCH ARTICLE

NANO · MICRO small
www.small-journal.com

High-Temperature Melt Stamping of Polymers Using Polymer/Nanoporous Gold Composite Stamps

*Ruža Periz, Markus Geuß, Nadiia Mameka, Jürgen Markmann, and Martin Steinhart**

Parallel lithographic deposition of polymers onto counterpart substrates is a widely applied surface manufacturing operation. However, polymers may only be soluble in organic solvents or are insoluble at all. Solvent evaporation during stamping may trigger hardly controllable capillarity-driven flow processes or phase separation, and polymer solutions may spread on the counterpart substrates. Solvent-free stamping of melts prevents these drawbacks. Here, a stamp design for the deposition of melts is devised, which intrinsically circumvents ink depletion. The stamps' topographically patterned contact surfaces with protruding contact elements contacting the counterpart substrates consist of a nanoporous gold layer with a thickness of a few micrometers. The nanoporous gold layer is attached to a molten polymer layer, which is support for the nanoporous gold layer and ink reservoir at the same time. The nanoporous gold layer in turn stabilizes the topography of the stamps' contact surfaces. As examples, arrays of submicron microdots of polystyrene and poly(vinylidenefluoride-trifluoroethylene) (PVDF-TrFE) are manufactured. The P(VDF-TrFE) microdots are partially crystalline, ferroelectric, and can be locally poled. It is envisioned that the methodology reported here can be automatized and may be extended to functional low-molecular-mass compounds, such as active pharmaceutical ingredients.

1. Introduction

The application of polymeric microstructures in areas such as sensing, energy storage, and soft robotics[1] as well as the printing of biologically relevant polymeric materials including curable synthetic polymers, synthetic gels, and naturally derived hydrogels[2] meets ongoing interest. Polymer microstructures may be formed by various methods.[3] Substrate manufacturing involving the deposition of polymers is commonly carried out using polymeric solutions as inks, such as in the case of capillary force lithography.[4] However, many polymers are only soluble in organic solvents, which might be volatile and/or hazardous. Other polymers might be hardly soluble at all. Furthermore, the desired polymeric surface structures form only after the evaporation of the solvent. Solvent evaporation is frequently accompanied by hardly controllable flow processes related to capillarity phenomena,[5,6] including the coffee ring effect,[7,8] or by liquid–liquid phase separation.[9] The deposited polymeric material may contain solvent residues, the removal of which by thermal annealing or application of a vacuum may damage the deposited polymer patterns. So far, only a limited number of methods potentially enable the solvent-free lithographic generation of polymer microstructures on counterpart substrates. Laser-induced forward transfer (LIFT)[10,11] is a serial pixel-by-pixel process; its ballistic nature may impede sufficient adhesion of the deposited material on the receiving counterpart substrates. Hot embossing[12,13] is a parallel technique involving the transfer of stamp topographies into pre-existing polymer layers; potential problems include heterogeneous contact pressure distribution and too strong adhesion between stamp and polymer substrate impeding stamp detachment. The solvent-free deposition of polymer microstructures onto receiving counterpart substrates using stamps was reported for some specific scenarios. Decal transfer microlithography involves the lithographic transfer of parts of polymeric stamps onto receiving counterpart substrates.[14] The disadvantage of this technique is the destruction of the stamps' contact surfaces in each single stamping step. Recently, high-temperature stamping of polymer melts with composite stamps consisting of a solid metal core coated with a relatively thin porous metal oxide layer was reported.[15] In this configuration, a limited amount of polymer melt is adsorbed to the porous oxide layer (cf. Figure S1, Supporting Information) for a schematic overview of strategies for the solvent-free deposition of polymer microstructures on receiving counterpart substrates based on the

R. Periz, M. Geuß, M. Steinhart
School of Biology and Chemistry and CellNanOs
Universität Osnabrück
Barbarastr. 7, 49076 Osnabrück, Germany
E-mail: martin.steinhart@uos.de

N. Mameka, J. Markmann
Helmholtz-Zentrum Hereon
Institute of Materials Mechanics
21502 Geesthacht, Germany

J. Markmann
Institute of Materials Physics and Technology
Hamburg University of Technology
21073 Hamburg, Germany

The ORCID identification number(s) for the author(s) of this article can be found under https://doi.org/10.1002/smll.202308478

DOI: 10.1002/smll.202308478

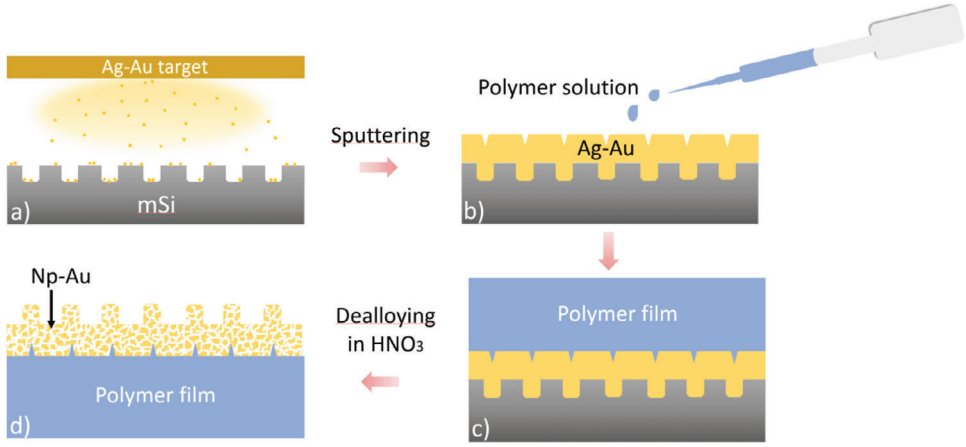

Figure 1. Schematic diagram of the preparation of polymer/npAu composite stamps. a) Ag–Au alloy (yellow) is deposited on macroporous silicon (mSi, gray). b) Polymer solution (blue) is drop-cast onto the exposed surface of the Ag–Au alloy. c) The polymer solidifies as the solvent evaporates. d) Treatment of the polymer/Ag–Au/mSi composite with HNO_3 solution leads to pore formation in the Ag–Au layer by dealloying and simultaneously to detachment of the forming polymer/npAu stamp from the mSi.

use of stamps). It is thus desirable to expand the procedures available for the parallel lithographic high-temperature deposition of polymer melts by approaches securing continuous replenishment of the polymer melt *in operando*.

Here, we present a design for high-temperature capillary stamping of polymer melts, in which the viscous polymer melts are used as ink reservoir and as support for a topographically patterned nanoporous gold (npAu) layer (**Figures 1** and **2**). The npAu layer separates the bulk melt of the polymer to be deposited and the receiving counterpart substrate to be patterned. Moreover, the npAu layer shapes the contact surface of the bulk polymer melt. The latter permeates the nanopores of the npAu layer and is deposited on the receiving counterpart substrate in the areas contacted by the protruding contact elements of the topographically structured npAu layer. In this way, polymers can be lithographically deposited on counterpart substrates without solvents. Moreover, ink depletion in the course of successive stamping steps, an intrinsic drawback of classical microcontact printing with solid elastomeric stamps, is inherently circumvented by the approach reported here.

For a proof of concept, we selected atactic polystyrene (PS) and poly(vinylidene difluoride-trifluoroethylene) P(VDF-TrFE) as model polymers. Atactic, entangled PS was selected because it is a well characterized, amorphous model polymer with a high glass transition temperature of ≈100 °C,[16] which is commercially available with narrow molecular mass distributions. Arrays of PS droplets were generated by methods such as surface-directed dewetting requiring substrates chemically prepatterned with areas of different surface energies.[17,18] PS droplets generated by surface-directed dewetting were used as etch resists in the topographical patterning of the underlying substrates. However, for this purpose, surface coatings reducing the surface energy in substrate areas not covered by PS need to be removed by additional process steps. Ferroelectric polymers,[19] in particular poly(vinylidene difluoride) (PVDF)[20] and its copolymers,[21,22] such as P(VDF-TrFE),[23] are used for actuators, smart sensors,[24] or as dielectrics with high permittivity for electric energy storage.[25,26] Consequently, micro- and nanostructured piezoelectric polymer structures accessible by, for example, electrospinning, template-assisted processes and molding, have received significant interest.[27–30] Polarization switching was, for example, demonstrated for ferroelectric P(VDF-TrFE) copolymer nanodots fabricated by dip-pen lithography[31] and by imprint lithography[32,33] as well as for crystalline nanodots in amorphous P(VDF-TrFE) films generated by local heating with AFM cantilever tips.[34]

2. Results

2.1. Generic Concept

The algorithm applied to prepare the polymer/npAu composite stamps is shown in Figure 1. We used macroporous silicon (mSi) containing macropores with a depth of 600 nm arranged in a hexagonal array with a lattice constant of 1.5 µm (Figure S2, Supporting Information)[35,36] as a master template. The macropores had a diameter of 900 nm at their mouths and of 600 nm at their bottoms. The mSi was then silanized with dimethyldichlorosilane (DMDCS). Next, ≈2.7 µm thick Ag–Au alloy layers were deposited on the DMDCS-coated mSi master templates using a direct current (DC) magnetron sputtering source equipped with an $Ag_{68}Au_{32}$ alloy target (Figure 1a; Figure S3, Supporting Information). Then, a solution of the polymer to be stamped was deposited on the exposed, topographically patterned Ag–Au surface (Figure 1b). The polymer solidifies as the solvent evaporates (Figure 1c). The use of polymer solutions at this stage is unproblematic because, if required, the content of residual solvent in the polymer layer can be reduced by application of a vacuum or by annealing without impairing subsequent process steps. Subsequent dealloying[37,38] with aqueous HNO_3 solutions converted the Ag–Au alloy layers of the polymer/Ag–Au/mSi composites into npAu. At the same time, the forming polymer/npAu composite stamps detached from the mSi (Figure 1d). Figure 2a,b shows scanning electron microscopy (SEM) images of the topographically patterned npAu surface of a PS/npAu composite stamp, which was initially in contact with the DMDCS-coated

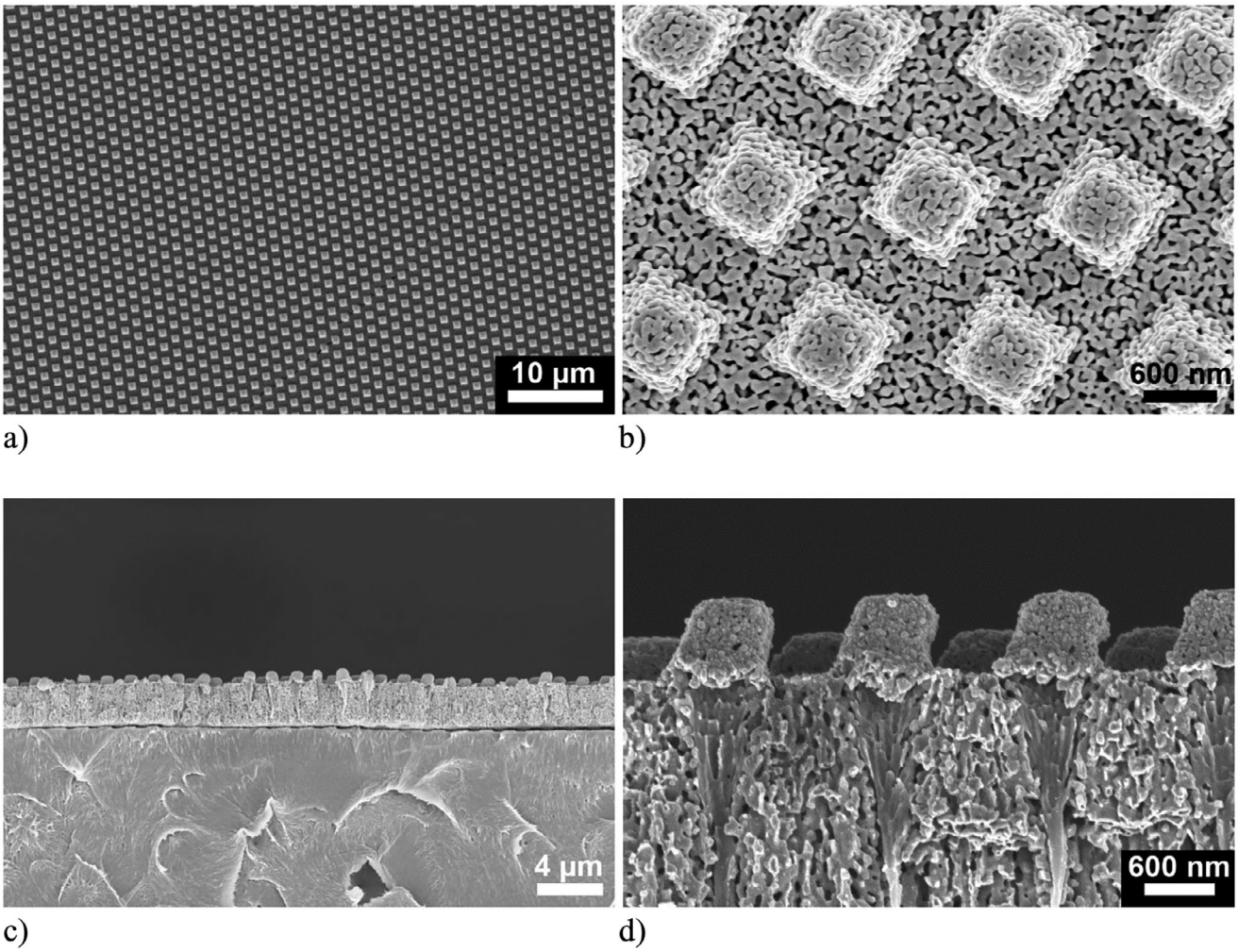

Figure 2. Scanning electron microscopy (SEM) images of PS/npAu composite stamps prior to any heating step. a,b) Top views of the topographically patterned npAu contact surface exhibiting protruding contact elements, which are replica of the mSi macropores. c) Cross-sectional view; the topographically patterned npAu layer is located in the center and the supporting PS layer at the bottom. d) Detail of a cross-section showing the npAu layer.

mSi surface. Cross-sectional SEM images of a PS/npAu stamp are displayed in Figure 2c,d. The npAu layers are negative replicas of the mSi master templates. Thus, the npAu layers possess protruding rod-like contact elements, which are negative replicas of the mSi macropores. The npAu layers are penetrated by spongy-continuous pore systems with pore diameters of a few 10 nm. At this stage, the npAu pores are not filled with polymer, because the polymer is already solidified when the npAu forms. The spike-like features seen in Figure 2d may be rationalized as follows. As obvious from Figure S3 (Supporting Information), prior to the dealloying the as-deposited Ag–Au layers exhibit narrow channels oriented normal to the layer plane at the positions of the rod-like contact elements, that is, at the former positions of the mSi macropores. We assume that during the sputtering of the Ag–Au alloy onto the mSi the Ag–Au is predominantly deposited on the rims bordering the mSi macropores, resulting in the formation of the channels at the positions of the mSi macropores. When, in the next step, PS is deposited on the exposed, topographically patterned Ag–Au surface, the PS fills these channels. During the preparation of the cross-sectional specimens shown in Figure 2, the PS located in the channels is stretched and forms the spike-like structures apparent in Figure 2d.

Figure 3 schematically summarizes high-temperature capillary stamping. An as-prepared polymer/npAu composite stamp (Figure 3a) is placed in a furnace (for details see Figure S4, Supporting Information). If an atactic, noncrystallizable polymer is used, the polymer/npAu composite stamp is heated to a target temperature well above the polymer's glass transition temperature T_g. If a partially crystalline polymer is used, the polymer/npAu composite stamp is heated to a temperature above the polymer's melting temperature T_m. Once the polymer is liquid, it infiltrates the spongy-mesoporous pore system of the npAu layer. If a polymer melt infiltrates a nanoporous host, the movement of the imbibition front measured as linear distance to the surface of the nanoporous host is smaller for a spongy-bicontinuous pore morphology than for arrays for straight cylindrical nanopores.[39] However, sufficiently stable stamp surfaces combining a tailored topography with arrays of straight

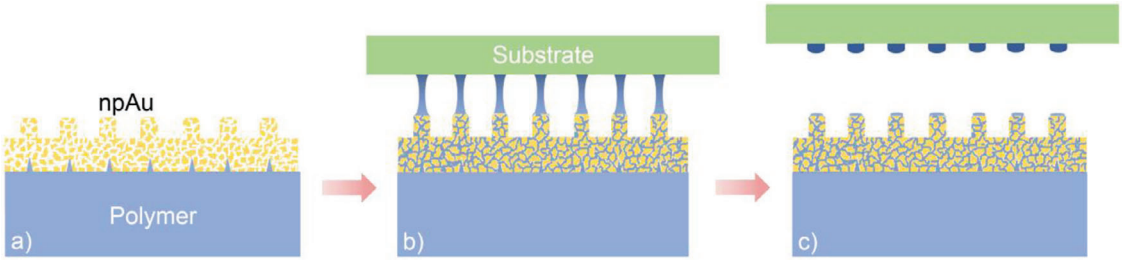

Figure 3. High-temperature capillary stamping with polymer/npAu composite stamps. a) A polymer/npAu composite stamp is b) heated to a target temperature, where the polymer (blue) is molten and infiltrates the npAu (yellow). If a receiving counterpart substrate (green) is approached to the polymer-infiltrated npAu surface, liquid polymer bridges form between the counterpart substrate and the contact elements of the polymer/npAu composite stamp (the length of the liquid bridges is exaggerated for better discernibility). c) Upon retraction of the receiving counterpart substrate from the polymer/npAu stamp still heated to the target temperature the liquid polymer bridges rupture, and polymer microdots remain on the receiving counterpart substrate.

cylindrical nanopores oriented perpendicularly to the plane of the stamp surface are hardly accessible. The architecture of the polymer/npAu composite stamps is nevertheless advantageous because the npAu layer supported by a molten yet sufficiently viscous polymer layer can have a thickness as low as a few µm (here <3 µm). Such thin layers with a spongy-continuous pore system are infiltrated even by entangled PS melts within a few minutes.[39] The receiving counterpart substrate to be patterned is placed on the exposed, topographically patterned npAu surface of the polymer/npAu composite stamp heated to the target temperature. Thus, liquid bridges form between the stamp's protruding contact elements and the receiving counterpart substrate (Figure 3b). The formation of focal contacts between the stamp's contact elements and the receiving counterpart substrate can be supported by placing a weight on top of the receiving counterpart substrate. After an adjustable dwell time, the receiving counterpart substrate is detached from the polymer/npAu composite stamp, while the latter is still heated to the target temperature. During the detachment, the polymer is thus still liquid. Upon detachment, the liquid polymer bridges connecting the contact elements of the polymer/npAu composite stamp and the receiving counterpart substrate rupture in such a way that polymer microdots remain attached to the receiving counterpart substrate at the positions of the liquid bridges (Figure 3c). The – now patterned – receiving counterpart substrate is removed from the furnace and allowed to cool to room temperature under ambient conditions. The polymer/npAu composite stamp remains located in the furnace and is still heated to the target temperature so that the stamping procedure can be repeated with new receiving counterpart substrates.

2.2. High-Temperature Capillary Stamping with PS/npAu Composite Stamps

We used atactic PS unable to crystallize and with narrow molecular mass distribution as the first model polymer because PS is likely the most intensively studied synthetic polymer. We brought PS/npAu composite stamps at a temperature of 200 °C in contact with glass slides used as receiving counterpart substrates. In the relevant temperature range, the PS used here (M_w = 239 000 g mol^{-1}; M_n = 233 000 g mol^{-1}; PDI = 1.02) forms ≈13 entanglements in bulk melts.[40,41] Said PS was shown to form a "dead layer" of PS chains immobilized on the hydroxyl-terminated oxidic surfaces of self-ordered anodic alumina.[42] "Dead layers" are assumed to reduce the effective pore radius of a porous medium infiltrated by a polymer melt. In turn, they cause an increase in the polymer melt's effective fluid viscosity and consequently a decrease in the infiltration speed.[43,44] However, on Au surfaces in contact with molten PS, PS precursor films with a thickness in the nm range far below the radii of gyration, which presumably consist of highly stretched PS chains, were observed.[45,46] In line with this finding, the passage of PS chains through the npAu layer is apparently not a limiting factor.

As discussed below, polymeric microdots were obtained after contact times of 60 s (the shortest contact time practicable with the setup used here). However, we also applied long contact times up to 30 min to evaluate whether spreading of the stamped polymer melts results in the formation of continuous polymer films no longer replicating the topographic patterns of the contact surfaces of the polymer/npAu composite stamps. **Figure** 4a–d shows exemplarily PS microdots obtained by contacting a glass slide with a PS/npAu composite stamp for 17 min at 200 °C (see Figure S5, Supporting Information, for large-field SEM images of arrays of PS microdots and Figure S6, Supporting Information, for a SEM image showing PS microdots at high magnification). Histograms of the PS microdot diameters, which we extracted from SEM images, are displayed in Figure 4e. The average diameters of the PS microdots obtained with dwell times ranging from 5 to 30 min lay in the range from 813 to 967 nm with standard deviations of ≈60 nm (for the detailed values see Table S1, Supporting Information). Histograms of the heights of the PS microdot diameters, which we extracted from AFM images, are displayed in Figure 4f. The average heights lay between 33 and 81 nm with standard deviations ranging from 6 to 10 nm (for the detailed values see Table S2, Supporting Information). Neither for the diameters nor for the heights of the PS microdots a systematic correlation with the dwell time was apparent.

To estimate the contact angles of PS microdots obtained with a dwell time of 30 min, we evaluated topographic line scans extracted from an AFM image. We thus determined 12 contact angles on 11 PS microdots and obtained an arithmetic mean value

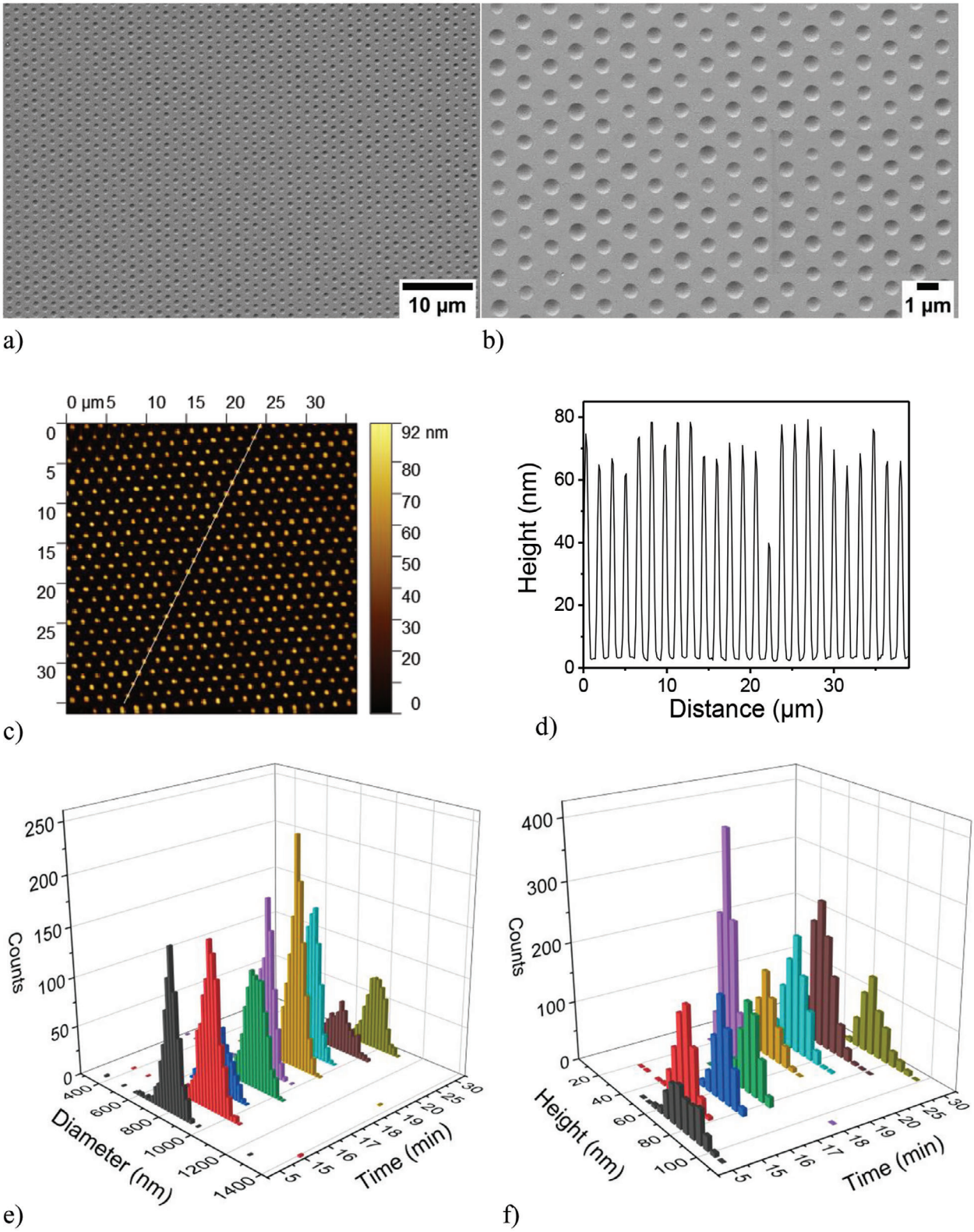

Figure 4. PS microdots deposited onto glass substrates by high-temperature capillary stamping with PS/npAu composite stamps at 200 °C. a) Large-field SEM image, b) higher-magnification SEM image and c) atomic force microscopy (AFM) topography image of PS microdots obtained with a dwell time of 17 min. d) Topographic height profile along the white line in panel (c). e,f) Histograms of e) the diameters of PS microdots obtained by evaluation of SEM images and f) the heights of PS microdots obtained by evaluation of AFM topography images for different dwell times (5 min, black; 15 min, red; 16 min, blue; 17 min, green, 18 min, purple; 19 min, mustard yellow; 20 min, light blue; 25 min, brown and 30 min, navy green).

of 10° ± 2°. However, this value should be interpreted with all due caution because the design of our experiments was not optimized with respect to accurate contact angle measurements. Moreover, apparent contact angles may vary with the resolution of the method applied to measure them. Schune et al. reported contact angles of ≈17° obtained from topographic AFM profiles for oligostyrene microdroplets on hydrophilic silicon wafers with a water contact angle of 0°;[47] the oligostyrene microdroplets had similar sizes than the PS microdots we obtained by high-temperature capillary stamping. However, Lau and Burns obtained macroscopic PS contact angles amounting to ≈50° from photographs of droplets of unentangled molten PS deposited onto a counterpart substrate.[48] Using a solution-based preparation strategy, Wang et al. obtained PS microparticles on glass with relatively high contact angles. Thermal annealing for 30 min (comparable to the longest dwell times we applied) yielded microlenses with smaller contact angles, which decreased as the annealing temperature was increased. For annealing temperatures of 150 °C and above, contact angles of ≈50 °C were obtained, as determined by AFM.[49]

2.3. High-Temperature Capillary Stamping with P(VDF-TrFE)/npAu Composite Stamps

We stamped P(VDF-TrFE) microdots onto Al-coated Si wafers and glass slides using P(VDF-TrFE)/npAu composite stamps at a stamping temperature of 205 °C applying dwell times ranging from 60 s to 30 min. Again, independent of the dwell time, we obtained discrete P(VDF-TrFE) microdots in all experiments. In contrast to the PS microdots obtained with PS/npAu composite stamps, the P(VDF-TrFE) microdots exhibited a corrugated surface (**Figure 5**; Figure S7, Supporting Information), which we interpret as a signature of crystalline P(VDF-TrFE) lamellae having edge-on orientation with respect to the receiving counterpart substrate. In the following, we will focus on P(VDF-TrFE) microdots stamped on Al-coated Si wafers since this substrate type enables the characterization of the P(VDF-TrFE) microdots by piezoresponse force microscopy (PFM).[50,51] PFM is a scanning probe microscopy technique that involves the application of a voltage between the cantilever tip and a counterpart substrate, both of which are coated with metal. Thus, the piezoresponse of sample materials in between can be detected so that ferroelectricity can be probed on the nanoscale. The P(VDF-TrFE) microdots stamped on Al-coated Si wafers with dwell times varied from 1 to 20 min had average diameters ranging from 872 to 1147 nm with standard deviations of a few tens of nm (Figure S8; for the detailed values see Table S3, Supporting Information). The average heights of the P(VDF-TrFE) microdots ranged from 39 to 77 nm with standard deviations lying between 10 and 20 nm (Figure S9; for the detailed values see Table S4, Supporting Information).

Figure 6a,b) shows a larger-area topography atomic force microscopy (AFM) image and a corresponding topographic height profile of P(VDF-TrFE) microdots stamped on an Al-coated Si waver applying a dwell time of 20 min. We studied the out-of-plane (OOP) piezoresponse of two P(VDF-TrFE) microdots normal to the surface of the Al-coated Si wafers by OOP-PFM. We applied voltage pulses of −15 V for 300 ms to both P(VDF-TrFE) microdots by placing the cantilever tip on their surface, followed by OOP-PFM phase imaging. In the obtained OOP-PFM image (Figure 6c) each of the two the P(VDF-TrFE) microdots shows a poled domain apparent as a dark area (inside the dashed red circles). Then, we positioned the cantilever tip again on the dark, prepoled domains of the P(VDF-TrFE) microdots and applied a second voltage pulse with a reversed voltage of +15 V for 300 ms. As apparent from the OOP-PFM image recorded afterward (Figure 6d), the second voltage pulse resulted in polarization reversal in the P(VDF-TrFE) microdots. In lieu of the previously dark domains now bright domains marked by red arrows in Figure 6d exist. Figure 6e shows the magnitude and Figure 6f the phase of pulse OOP-PFM hysteresis loops measured in the center of the left P(VDF-TrFE microdot in Figure 6c,d. The PFM

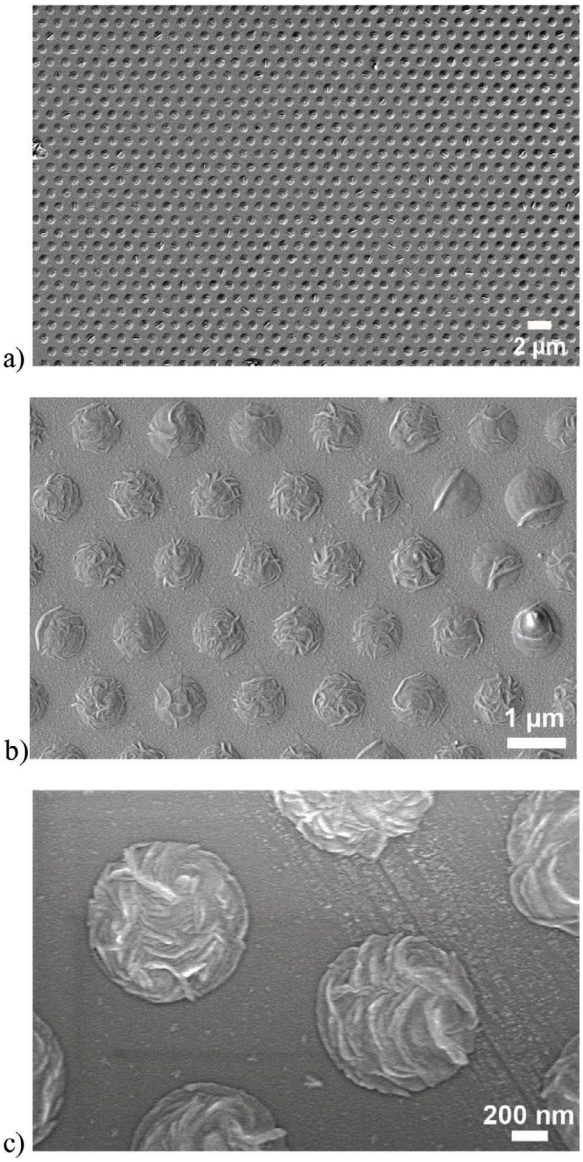

Figure 5. SEM images of P(VDF-TrFE) microdots formed by high-temperature capillary stamping at 205 °C using P(VDF-TrFE)/npAu composite stamps. a) Receiving counterpart substrate: glass; dwell time: 20 min. b) Receiving counterpart substrate: Al-coated Si wafer; dwell time: 2 min. c) Receiving counterpart substrate: glass; dwell time: 17 min.

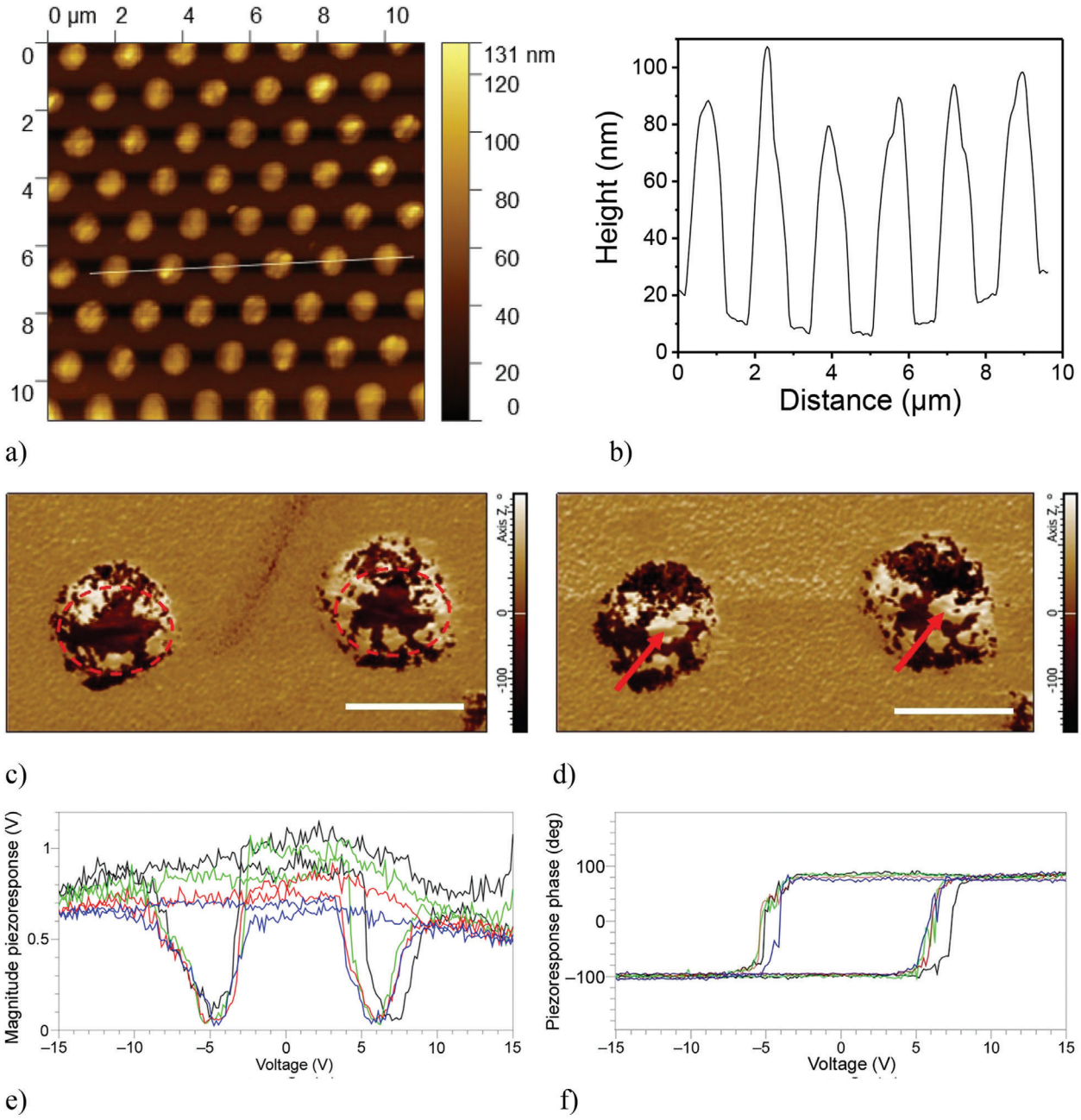

Figure 6. AFM and out-of-plane piezoresponse force microscopy (OOP-PFM) characterization of P(VDF-TrFE) microdots deposited onto an Al-coated Si wafer by high-temperature capillary stamping with a P(VDF-TrFE)/npAu composite stamp (dwell time 20 min). a) Large-area AFM topography image and b) topographical profile along the white line in panel (a). c) OOP-PFM phase image of two individual P(VDF-TrFE) microdots after applying −15 V for 300 ms showing prepoled areas (dark domains inside the dashed red circles). d) OOP-PFM phase image of the same area as in (c) after applying +15 V for 300 ms showing polarization reversal (bright domains marked by the red arrows). The lengths of the scale bars in (c) and (d) correspond to 500 nm. e) Magnitude and f) phase of pulse OOP-PFM hysteresis loops (black, 1st cycle; green, 2nd cycle; red, 3rd cycle; blue, 4th cycle) measured in the center of the left P(VDF-TrFE) microdot in panels c) and d).

results confirm that the P(VDF-TrFE) microdots are polycrystalline and exhibit full ferroelectric switching behavior. The shape of the hysteresis loops indicates high crystallinity.

Some P(VDF-TrFE) microdot arrays locally contained small regions in which the P(VDF-TrFE) microdots had smaller diameters of ≈200 nm or even below (Figure S10, Supporting Information). We assume that the cutting into smaller pieces (see section "4.6 Stamping Procedures" below) resulted in bending of the polymer/npAu composite stamps. The bent parts may form in turn imperfect contact with the receiving counterpart substrates. Notably, we were able to pole P(VDF-TrFE) microdots with diameters in the 200 nm range and to measure ferroelectric hysteresis

loops (Figures S11 and S12, Supporting Information). This outcome evidences that even this population of smaller P(VDF-TrFE) microdots is highly crystalline and ferroelectric.

3. Discussion

3.1. Wettability of the Receiving Counterpart Substrates

In the course of high-temperature capillary stamping, the contact elements of the polymer/npAu composite stamps are in contact with an excess bulk reservoir of molten polymer. Thus, in principle an "infinite" amount of polymer could be transferred from the contact elements to the receiving counterpart substrate. However, even after extended dwell times of up to 30 min apparently discrete polymer microdots were obtained, the diameters of which were similar to those obtained for any shorter dwell time. The transfer of polymer from the bulk reservoir to the receiving counterpart substrate will, on the one hand, be influenced by the viscosity and the rheology of the polymer. On the other hand, the wetting behavior of the transferred polymer on the receiving counterpart substrate will crucially impact the outcome of high-temperature capillary stamping. The assessment of surface wettability by the measurement of contact angles is impeded by the complexity of the underlying physics. Contact angles are phenomenologically observed on non-ideal real-life substrates, which are inevitably heterogeneous. Thus, measured contact angles do not correspond to the Young contact angles and should be referred to apparent contact angles,[52,53] which at best average over local equilibrium contact angles but likely represent metastable wetting configurations. Apparent contact angles are, for example, influenced by local configurations of the three-phase contact line defining the contour of a probed portion of liquid, the existence of a broad range of metastable local and global wetting configurations associated with a multitude of different contact angle values, as well as the dependence of the contact angles on the volumes of the probed liquid droplets.[54–56] The smaller a droplet is as compared to surface heterogeneities, the more likely is the droplet trapped in a metastable state deviating from the thermodynamic equilibrium.[57] Since the polymer microdots obtained here by high-temperature capillary stamping have diameters in the submicron range, it is reasonable to assume that their phenomenology is influenced by metastable configurations of their three-phase contact lines. Furthermore, liquid polymer bridges with two principal curvatures exist between the receiving counterpart substrate and the contact elements of the polymer/npAu composite stamp, and the molten polymer likely forms menisci at the pore openings of the contact elements. Hence, the Laplace pressure at the curved polymer-air interfaces and Laplace pressure differences might also influence the wetting behavior of the transferred polymer on the receiving counterpart substrate. We assume that the spreading of the polymer in the course of high-temperature capillary stamping presumably comes to a halt when the energy required to pass surface heterogeneities on the receiving counterpart substrate plus the energy required to pull polymer out of the contact elements of the polymer/npAu composite stamp exceed the energy of adhesion gained when the surface area on the receiving counterpart substrate covered by polymer increases.

Contamination of the receiving counterpart substrates may also influence their wettability. For example, the receiving counterpart glass substrates used here have a hydroxyl-terminated high-energy surface, on which any liquid should spread. However, under the conditions high-temperature capillary stamping is carried out, it is likely that organic contaminations, including the ethanol used for the cleaning of the glass substrates, are adsorbed to the surface of the latter. These adsorbates may reduce the wettability of the glass substrates, resulting in the observed invariant shape of discrete PS microdots even for extended dwell times. Potentially, pseudo-partial wetting may also play a role. The equilibrium in the pseudo-partial wetting regime is characterized by persistent droplets with nonzero contact angles coexisting with their precursor films.[58,59] The latter typically have a thickness of the order of a nanometer or below. Indeed, pseudo-partial wetting of molten PS (albeit with a low molecular mass) on silica surfaces was reported in a previous study.[47] Dewetting of low-molecular-mass PS on silica surfaces yielded similar structures, indicating that on high-energy surfaces PS droplets surrounded by nm-thin PS wetting films are an equilibrium configuration.[58] In any case, high-temperature capillary stamping of viscous, entangled polymer melts, such as the PS used here, seems to prevent ink spreading on unmodified oxidic and metallic surfaces. We assume that the contour of the stamped features is most efficiently adjusted by the size and the shape of the stamps' contact elements, as demonstrated for porous stamps used to deposit solution-based inks.[60] It should also be noted that chemical surface modification, for example by silanes or thiols, to tune the surface wettability of the receiving counterpart substrate might be not feasible in the context of high-temperature capillary stamping since the surface modification might not be stable at the applied temperatures. Furthermore, we did not find systematic differences in the diameters of P(VDF-TrFE) microdots stamped on Al-coated Si wafers (Table S3 and Figure S8, Supporting Information) and on glass substrates (Table S5 and Figure S13, Supporting Information). We assume that the surface of the Al coating consists of a thin native alumina layer so that the Al-coated Si wafers have surface properties comparable to those of the glass substrates.

3.2. Potential of the Automatization of High-Temperature Capillary Stamping

The heights of the polymer microdots obtained by high-temperature capillary stamping with polymer/npAu composite stamps are at least one order of magnitude larger than those of patterns obtained by room-temperature capillary stamping of polymeric solutions.[61] The speed at which the receiving counterpart substrate is retracted will crucially determine how the polymer is distributed between the receiving counterpart substrate and the contact elements of the polymer/npAu composite stamp. The retraction speed was identified as an important parameter of dip pen nanolithography.[62] In the case of entangled liquid polymers subjected to uniaxial extension, irreversible viscous deformations prevail at low deformation rates and rupture may be triggered by instabilities related to surface tension. At high deformation rates, entangled polymers behave like rubbers.[63] Thus, the scattering of the heights of the polymer microdots

obtained by high-temperature capillary stamping is presumably related to the manual detachment of the receiving counterpart substrates from the contact surface of the polymer/npAu composite stamps. Manual detachment allows only limited control of the way how the liquid polymer bridges connecting the contact elements of the polymer/npAu composite stamp and the receiving counterpart substrate rupture. In our manual operation mode, we used the polymer/npAu composite stamps for at least 7 to 10 stamping cycles. However, it should be noted that parts of the contact elements of the polymer/npAu composite stamps and even portions of the bulk polymer may remain attached to the receiving counterpart substrates, if the manual retraction of the latter is performed too vigorously (Figure S14, Supporting Information). These problems might be avoided by the automatization of high-temperature capillary stamping similar to polymer pen lithography with stamps having rigid contact elements[64] and the scenario reported Hou et al.[65] The polymer/npAu composite stamps would be permanently kept at the target stamping temperature, while the receiving counterpart substrates to be patterned were automatically approached and retracted after dwell times of a few tens of seconds. Thus, high-temperature capillary stamping could be performed applying automated leveling procedures, well-controlled approach, and retraction speeds as well as well-controlled contact pressures (the force per area applied to press the receiving counterpart substrate onto the contact surface of the polymer/npAu composite stamp). The occasionally observed variations in the size of P(VDF-TrFE) microdots, which we attribute to areas of the polymer/npAu composite stamps deformed by cutting, suggest that varying the contact pressure may allow for varying the amount of polymer transferred per contact element to the receiving counterpart substrates. On the other hand, well-controlled retraction speeds may allow for controlling how the liquid polymer bridges connecting the stamps' contact elements and the receiving counterpart substrates rupture and, therefore, for controlling how the polymer forming the liquid bridges is distributed between the receiving counterpart substrates and the contact elements.

4. Conclusion

We have introduced a design for polymer/nanoporous gold composite stamps, which enables lithographic deposition of molten polymers at elevated temperatures onto receiving counterpart substrates. A molten polymer layer is both the ink reservoir and the support for a thin, topographically structured nanoporous gold layer. The topographically structured nanoporous gold layer forming contact to the counterpart substrate is thin enough to allow permeation of the polymer chains to the counterpart substrate. On the other hand, the nanoporous gold layer stabilizes the topography of the contact surface of the polymer/nanoporous gold composite stamps patterned with protruding contact elements. Thus, micropatterns of molten polymers, such as arrays of microdots, with heights of several 10 nm can be stamped onto receiving counterpart substrates without ink depletion. Even on high-energy surfaces[66] the polymer melts do not spread but form discrete 3D microdots. Using melts of entangled atactic PS with narrow molecular mass distribution and of the ferroelectric polymer P(VDF-TrFE) as model inks, we found that the microdot sizes and volumes do not depend on the dwell times varied from 60 s to 30 min. The shapes of the polymer microdots appear to be related to the shape of the protruding contact elements of the polymer/npAu composite stamps. As it is commonly the case for stamp-based contact-lithographic methods, the main lever to modify the contours of the deposited features would be a correspondingly modified topography of the contact surfaces of the stamps (for porous stamps see, for example, Guo and Steinhart[60]).

The P(VDF-TrFE) microdots obtained with P(VDF-TrFE)/npAu composite stamps were semicrystalline and showed pronounced ferroelectric behavior. High-temperature capillary stamping of polymer melts is an extension of the existing portfolio of lithographic surface patterning methods. The applicability of high-temperature capillary stamping is certainly restricted to certain temperature/molecular mass windows if melts of entangled polymers are used as inks. This approach nevertheless circumvents potential problems related to the use of polymeric solutions as inks, including poor solubility of the polymeric components, use of organic solvents, hardly controllable processes triggered by solvent evaporation such as phase separation and capillary flow phenomena, the presence of residual solvent in the stamped patterns and small amounts of deposited material. We also envision that high-temperature capillary stamping can be extended to melts of organic compounds including active pharmaceutical ingredients. We moreover envision that drawbacks related to the fully manual procedures reported here may be overcome by the automatization of high-temperature capillary stamping involving well-controlled leveling procedures, temperature control, approach speeds, and retraction speeds.

5. Experimental Section

Materials and Chemicals: Macroporous silicon (mSi) with macropores arranged in hexagonal arrays with a lattice constant of 1.5 µm[35,36] was obtained from Smart membranes (Halle/Saale, Germany). The macropores had a pore depth of 600 nm. The diameter of the macropores amounted to ≈900 nm at their pore mouths and to ≈600 at their bottoms. Cover glass substrates were purchased from Th. Geyer GmbH. Dimethyldichlorosilane (DMDCS) was obtained from Merck, 2-butanone from Fluka, *n*-hexane (>95%) from Fisher Chemical, and nitric acid (64–66%) as well as toluene from Sigma–Aldrich. Polystyrene (M_w = 239 000 g mol^{-1}; M_n = 233 000 g mol^{-1}; PDI = 1.02) was supplied by Polymer Standards Service (Mainz, Germany). Poly(vinylidenefluoride-*stat*-trifluoroethylene) (PVDF-TrFE) (M_w = 209 740 g mol^{-1}; M_n = 100 008 g mol^{-1}; PDI = 2.09)[67] was supplied by Piezotech SA (France).

Stamp Preparation – Generic Steps: Macroporous silicon cut into pieces extending 1 × 1 cm^2 was treated with a mixture of 500 µL DMDCS and 9.5 g *n*-hexane at 40 °C for 24 h and then washed with ethanol. The deposition of Ag–Au films onto DMDCS-coated macroporous silicon pieces was carried out by DC magnetron sputtering (custom made device with a base pressure <10^{-7} mbar, BESTEC) using Ag–Au targets (purity 99.99%) containing 68 mol-% Ag and 32 mol-% Au corresponding to 54 wt-% Au and 46 wt-% Ag on a rotating sample holder. The DC magnetron sputtering was carried out at 50 W in the power regulation mode with a target distance of 7 cm. The base pressure of the device was set to 5.7 × 10^{-3} mbar under gas flow (7 sccm Argon 5.0). After 90 min deposition time with a deposition rate of 30 nm min^{-1}, a ≈2.7 µm thick Ag–Au film was obtained.

Preparation of PS/npAu Composite Stamps: PS (0.1 g) was dissolved in 1 mL toluene and left overnight in a shaker at 300 rpm. 60 µL solution was dropped onto the Ag–Au surface of the Ag–Au-coated macroporous silicon seven times with a wait time of 30 min between the deposition steps. Thus, overall 420 µL solution was deposited, resulting in the

formation of PS films with a thicknesses of ≈400 µm. The samples were then annealed for 18 h at 200 °C and then for 5 h at 210 °C in Ar atmosphere. For dealloying, PS/Ag-Au/mSi-PS samples were immersed in 15 mL of a 21.7% HNO_3 solution. Dealloying lasted from 24 h until 2 weeks, depending on the individual sample. The required dealloying time was different for each stamp. The dealloying process started at the edges of the Ag–Au layers sandwiched between mSi and PS. In the course of the dealloying, the Ag–Au/PS composites spontaneously detached from the mSi. Only after detachment, the dealloying process proceeded on the whole metal surface of the Ag–Au/PS composites. Formation of the porosity throughout the Ag–Au layer was visually monitored. A color change from silver-gray to brown indicated completion of the dealloying. Subsequently, the obtained PS/npAu composite stamps were washed three times in water and dried at 40 °C for 24 h.

Preparation of P(VDF-TrFE)/npAu Composite Stamps: Ag-Au/mSi composite layers were treated two times with 200 µL 21.7% HNO_3 solution for ≈30 min. In between, the samples were rinsed with deionized water. After the second step, the Ag–Au/mSi composite layers were dried at 40 °C for ≈1 h. A solution of 0.1 g mL^{-1} P(VDF-TrFE) in 2-butanone was prepared by sonication at 60 °C for ≈40 min. 40 µL of this solution was dropped on the Ag–Au surface of the Ag–Au/mSi composites and left to dry for ≈30 min at room temperature. This step was repeated two times so that overall 120 µL solution was deposited. During the solvent evaporation, the Ag–Au/P(VDF-TrFE) composites separated from the mSi, which could thus be reused. The freestanding Ag–Au/P(VDF-TrFE) composites with ≈95 µm thick P(VDF-TrFE) films obtained in this way were annealed at 145 °C for 1 h in argon atmosphere to remove residual solvent. For dealloying, the Ag–Au/P(VDF-TrFE) composites were immersed in 15 mL of a 21.7% HNO_3 solution for 48 h at room temperature. The obtained P(VDF-TrFE)/npAu composite stamps were washed three times in water and dried at 40 °C for 24 h.

Treatment of Receiving Counterpart Substrates: The receiving counterpart substrates to be patterned with PS or P(VDF-TrFE) microdots by high-temperature capillary stamping were treated as follows. Cover glass slides (≈18 × 18 mm^2) with a thickness of 1 mm were cut into pieces with a size of ≈9 × 9 mm^2 and cleaned in an ultrasonic bath, first in distilled water for 30 min and then three times for 15 min in ethanol. Before use, these receiving counterpart substrates were dried in an argon flow. Silicon wafers as receiving counterpart substrates (size 9 × 9 mm^2) were cleaned in ethanol in an ultrasonic bath and coated with aluminum under a vacuum at 10^{-4} mbar in a thermal evaporator device Balzers BAE 120. Thus, Al coatings with a thickness exceeding 50 nm were obtained. Before use, the Al-coated Si wafers were cleaned in an argon stream for a few seconds.

Stamping Procedures: PS microdots were stamped on glass slides using the PS/npAu composite stamps and P(VDF-TrFE) microdots on glass slides and Al-coated Si substrates using the P(VDF-TrFE)/npAu composite stamps. Cover glass slides coated with gold (in three consecutive cycles lasting 15 s at 20 mA using a JEOL sputter coater) were put onto cylindrical stainless-steel stamp holders with a diameter of 3.5 cm located in home-made precision furnaces. The PS/npAu and P(VDF-TrFE)/npAu composite stamps with an initial size of 1 cm^2 were cut into smaller pieces extending ≈2 × 2 mm^2 with a scalpel. These pieces were placed on the gold-coated surfaces of the cover glass slides in such a way that their topographically patterned npAu surfaces were exposed and pointing upward, whereas the bulk polymer layers at the bottom were in contact with the gold-coated cover glass slides (cf. Figure S4, Supporting Information; the gold coating of the cover glass slides reduced adhesion of the polymer and facilitated the detachment of the polymer/npAu stamps during the disassembly of the stamping devices after completion of the stamping operations). Then, the furnaces were heated to the desired target temperature at a heating rate of 5 K min^{-1}. For all stamping experiments with PS/npAu composite stamps the target temperature was set at 200 °C and for all stamping experiments with P(VDF-TrFE)/npAu composite stamps at 205 °C. The furnaces were closed with a lid during the heating. The polymer/npAu composite stamps were kept at the target temperature for ≈20 min to make sure that the polymers infiltrated the npAu layers. Then, the lids of the furnaces were removed. Using tweezers, the receiving counterpart substrates to be patterned were placed onto the exposed npAu contact surfaces of the polymer/npAu composite stamps heated to the target temperature. Subsequently, cylindrical stainless-steel weights with a diameter of 2 cm, a height of 1.64 cm, and a mass of 40 g were located on top of the receiving counterpart substrates. The pressure thus applied to the polymer/npAu composite stamps amounted to ≈0.4 MPa. After the intended dwell time, the cylindrical stainless-steel weights were removed, and the receiving counterpart substrates were detached from the polymer/npAu stamps still heated to the target temperature using tweezers. The patterned receiving counterpart substrates were removed from the furnaces and cooled to room temperature under ambient conditions. The polymer/npAu composite stamps remained located in the furnace – still heated to the target temperature – and could be used for the next stamping procedure.

Atomic Force Microscopy (AFM) and Piezoresponse Force Microscopy (PFM): All AFM and PFM measurements were performed using a NT-MDT Ntegra device. AFM topography measurements were carried out in the tapping mode with aluminum-coated silicon cantilevers with force constants of 30–70 N m^{-1} (MikroMasch). P(VDF-TrFE) microdots stamped on aluminum-coated Si wafers were studied by PFM using Pt/Ir-coated CSG01 cantilevers (NanoAndMore, force constant typically 0.03 N m^{-1}). Imaging and local poling experiments (point poling and hysteresis loops) were performed by applying rectangular voltage pulses to the Al back electrode and AC voltage to the Pt/Ir-coated cantilever beams. Voltage pulses were amplified to the appropriate voltage using a homebuilt amplifier. Local hysteresis loops were recorded by applying rectangular voltage pulses having widths of 300 ms and 300 ms wait times with a triangular-shaped envelope of the pulse train. Only the out-of-plan (vertical) piezoresponse was further analyzed. P(VDF-TrFE) microdots were poled by the out-of-plane (OOP) PFM phase mode applying voltage pulses at −15 and +15 V with durations of 300 ms.

Scanning Electron Microscopy (SEM): For SEM investigations a Zeiss Auriga scanning electron microscope was used. SEM images were captured with InLens and secondary electron chamber detectors. For the imaging of the surfaces of the polymer/npAu composite stamps accelerating voltages of 7 or 15 kV were applied. Receiving counterpart substrates functionalized with stamped polymer microdots were coated with gold in three consecutive cycles at 20 mA for 15 s in a JEOL sputter coater or with platinum/iridium in three consecutive cycles at 20 mA for 15 s in an Emitech K575X sputter coater and then imaged at accelerating voltages of 3 or 15 kV.

Image Analysis: To compile frequency histograms of the polymer microdot diameters, SEM images were used containing as many polymer microdots as possible, while the pixel sizes of the polymer microdots were still large enough for a meaningful diameter analysis. On the other hand, the images to be evaluated must not contain macroscopic contrast gradients so that binarization without contrast saturation is possible. For each sample, one suitable SEM image was selected, binarized and analyzed using the software Fiji-ImageJ. The SEM images were binarized by choosing a brightness threshold value in a brightness range in which the image was invariant against small changes of the brightness threshold value. The binarized SEM images were used to determine the microdot areas. Microdot diameters were calculated from the microdot areas using the software OriginLab assuming a circular microdot shape. Exemplarily, the SEM image and its binarized version used to obtain a diameter frequency histogram for PS microdots obtained at 200 °C with a dwell time of 17 min are shown in Figure S15 (Supporting Information). In this case, 967 PS microdots with pixel diameters of ≈10 pixels were evaluated. The numbers of polymer microdots evaluated for the compilation of the microdot diameter frequency histograms are specified in Tables S1,S3, and S5 (Supporting Information).

Supporting Information

Supporting Information is available from the Wiley Online Library or from the author.

Acknowledgements

Open access funding enabled and organized by Projekt DEAL.

Conflict of Interest

The authors declare no conflict of interest.

Data Availability Statement

The data that support the findings of this study are available from the corresponding author upon reasonable request.

Keywords

ferroelectric microstructures, microcontact printing, nanoporous gold, polymer microdots, surface patterning

Received: September 23, 2023
Revised: January 5, 2024
Published online: January 23, 2024

[1] M. A. Rose, J. J. Bowen, S. A. Morin, *ChemPhysChem* **2019**, *20*, 909.
[2] A. Skardal, A. Atala, *Ann. Biomed. Eng.* **2015**, *43*, 730.
[3] M. Qiu, W. Du, S. Zhou, P. Cai, Y. Luo, X. Wang, R. Yang, J. Zhao, *Prog. Polym. Sci.* **2023**, *142*, 101688.
[4] D. Ho, J. Zou, B. Zdyrko, K. S. Iyer, I. Luzinov, *Nanoscale* **2015**, *7*, 401.
[5] A. Y. Malkin, *Colloid J.* **2008**, *70*, 673.
[6] R. V. Craster, O. K. Matar, *Rev. Mod. Phys.* **2009**, *81*, 1131.
[7] R. D. Deegan, O. Bakajin, T. F. Dupont, G. Huber, S. R. Nagel, T. A. Witten, *Nature* **1997**, *389*, 827.
[8] D. Mampallil, H. B. Eral, *Adv. Colloid Interface Sci.* **2018**, *252*, 38.
[9] P. Van de Witte, P. J. Dijkstra, J. W. A. Van Den Berg, J. Feijen, *J. Membr. Sci.* **1996**, *117*, 1.
[10] P. Serra, A. Pique, *Adv. Mater. Technol.* **2019**, *4*, 1800099.
[11] Z. Ur Rehman, F. Yang, M. Wang, T. Zhu, *Opt. Laser Technol.* **2023**, *160*, 109065.
[12] L. Peng, Y. Deng, P. Yi, X. Lai, *J. Micromech. Microeng.* **2014**, *24*, 013001.
[13] S. S. Deshmukh, A. Goswami, *Mater. Manuf. Process* **2021**, *36*, 501.
[14] W. R. Childs, R. G. Nuzzo, *J. Am. Chem. Soc.* **2002**, *124*, 13583.
[15] F. Alarslan, H. Hübner, J. Klein, K. Kupper, J. Wollschlager, M. Haase, M. Gallei, M. Steinhart, *ACS Appl. Polym. Mater.* **2023**, *5*, 5738.
[16] T. G. Fox, P. J. Flory, *J. Appl. Phys.* **1950**, *21*, 581.
[17] A. Sehgal, V. Ferreiro, J. F. Douglas, E. J. Amis, A. Karim, *Langmuir* **2002**, *18*, 7041.
[18] Z. Zhang, Z. Wang, R. Xing, Y. Han, *Polymer* **2003**, *44*, 3737.
[19] A. J. Lovinger, *Science* **1983**, *220*, 1115.
[20] D. M. Nivedhitha, S. Jeyanthi, *Polym. Adv. Technol.* **2023**, *34*, 474.
[21] F. J. B. Calleja, A. G. Arche, T. A. Ezquerra, C. S. Cruz, F. Batallan, B. Frick, E. L. Cabarcos, *Adv. Polym. Sci.* **1993**, *108*, 1.
[22] B. Ameduri, *Prog. Polym. Sci.* **2022**, *133*, 101591.
[23] J. F. Legrand, *Ferroelectrics* **1989**, *91*, 303.
[24] B. Stadlober, M. Zirkl, M. Irimia-Vladu, *Chem. Soc. Rev.* **2019**, *48*, 1787.
[25] J.-W. Zha, M.-S. Zheng, B.-H. Fan, Z.-M. Dang, *Nano Energy* **2021**, *89*, 106438.
[26] Q. K. Feng, S. L. Zhong, J. Y. Pei, Y. Zhao, D. L. Zhang, D. F. Liu, Y. X. Zhang, Z. M. Dang, *Chem. Rev.* **2022**, *122*, 3820.
[27] D. Guo, F. Zeng, B. Dkhil, *J. Nanosci. Nanotechnol.* **2014**, *14*, 2086.
[28] V. Cauda, G. Canavese, S. Stassi, *J. Appl. Polym. Sci.* **2015**, *132*, 41667.
[29] J.-H. Lee, H.-J. Yoon, T. Y. Kim, M. K. Gupta, J. H. Lee, W. Seung, H. Ryu, S.-W. Kim, *Adv. Funct. Mater.* **2015**, *25*, 3203.
[30] Y. Ahn, Y. H. Shin, J. Y. Son, *Appl. Phys. A* **2016**, *122*, 882.
[31] Y. Ahn, J. Y. Son, *Org. Electron.* **2017**, *41*, 205.
[32] X.-Z. Chen, Q. Li, X. Chen, X. Guo, H.-X. Ge, Y. Liu, Q.-D. Shen, *Adv. Funct. Mater.* **2013**, *23*, 3124.
[33] Y. Chen, M. Xu, X. Hu, Y. Yue, X. Zhang, Q. Shen, *Nanoscale* **2020**, *12*, 11997.
[34] J. Y. Son, I. Jung, Y.-H. Shin, *J. Phys. Chem. C* **2013**, *117*, 12890.
[35] V. Lehmann, H. Föll, *J. Electrochem. Soc.* **1990**, *137*, 653.
[36] A. Birner, U. Grüning, S. Ottow, A. Schneider, F. Müller, V. Lehmann, H. Föll, U. Gösele, *Phys. Status Solidi A* **1998**, *165*, 111.
[37] J. Erlebacher, M. J. Aziz, A. Karma, N. Dimitrov, K. Sieradzki, *Nature* **2001**, *410*, 450.
[38] I. McCue, E. Benn, B. Gaskey, J. Erlebacher, *Annu. Rev. Mater. Res.* **2016**, *46*, 263.
[39] F. V. Luna, A. K. Maurya, J. M. De Souza E Silva, G. Dittrich, T. Paul, D. Enke, P. Huber, R. Wehrspohn, M. Steinhart, *J. Phys. Chem. C* **2022**, *126*, 12765.
[40] S. Wu, *J. Polym. Sci., Part B: Polym. Phys.* **1989**, *27*, 723.
[41] L. J. Fetters, D. J. Lohse, S. T. Milner, W. W. Graessley, *Macromolecules* **1999**, *32*, 6847.
[42] F. Vazquez Luna, M. Gerstenberger, G. Dittrich, J. Martins De Souza E Silva, P. Huber, R. Wehrspohn, M. Steinhart, *J. Phys. Chem. C* **2021**, *125*, 26731.
[43] Y. Yao, S. Alexandris, F. Henrich, G. Auernhammer, M. Steinhart, H.-J. Butt, G. Floudas, *J. Chem. Phys.* **2017**, *146*, 203320.
[44] Y. Yao, H. J. Butt, G. Floudas, J. J. Zhou, M. Doi, *Macromol. Rapid Commun.* **2018**, *39*, 1800087.
[45] D. Glick, P. Thiansathaporn, R. Superfine, *Appl. Phys. Lett.* **1997**, *71*, 3513.
[46] R. D. Deshmukh, R. J. Composto, *Langmuir* **2007**, *23*, 13169.
[47] C. Schune, M. Yonger, B. Bresson, C. Fretigny, L. Guy, T. Chaussée, F. Lequeux, H. Montes, E. Verneuil, *Langmuir* **2019**, *35*, 7727.
[48] W. W. Y. Lau, C. M. Burns, *J. Colloid Interface Sci.* **1973**, *45*, 295.
[49] Y. Wang, B. Zeng, Y. Zhao, S. Li, X. Zhang, *J. Phys. Chem. C* **2019**, *123*, 14327.
[50] R. K. Vasudevan, N. Balke, P. Maksymovych, S. Jesse, S. V. Kalinin, *Appl. Phys. Rev.* **2017**, *4*, 021302.
[51] A. Gruverman, M. Alexe, D. Meier, *Nat. Commun.* **2019**, *10*, 1661.
[52] A. Marmur, C. Della Volpe, S. Siboni, A. Amirfazli, J. W. Drelich, *Surf. Innovations* **2017**, *5*, 3.
[53] J. W. Drelich, L. Boinovich, E. Chibowski, C. Della Volpe, L. Holysz, A. Marmur, S. Siboni, *Surf. Innovations* **2020**, *8*, 3.
[54] J. Drelich, J. D. Miller, J. Hupka, *J. Colloid Interface Sci.* **1993**, *155*, 379.
[55] C. H. Kung, P. K. Sow, B. Zahiri, W. Mérida, *Adv. Mater. Interfaces* **2019**, *6*, 1900839.
[56] N. Kubochkin, T. Gambaryan-Roisman, *Phys. Rev. E: Stat. Phys., Plasmas, Fluids, Relat. Interdiscip. Top.* **2021**, *6*, 093603.
[57] S. Brandon, N. Haimovich, E. Yeger, A. Marmur, *J. Colloid Interface Sci.* **2003**, *263*, 237.
[58] R. Seemann, S. Herminghaus, K. Jacobs, *Phys. Rev. Lett.* **2001**, *86*, 5534.
[59] F. Brochard-Wyart, J. M. Di Meglio, D. Quéré, P. G. De Gennes, *Langmuir* **1991**, *7*, 335.
[60] L. Guo, M. Steinhart, *Appl. Surf. Sci.* **2023**, *639*, 158209.
[61] M. Runge, H. Hübner, A. Grimm, G. Manoharan, R. Wieczorek, M. Philippi, W. Harneit, C. Meyer, D. Enke, M. Gallei, M. Steinhart, *Adv. Mater. Interfaces* **2021**, *8*, 2001911.

[62] D. J. Eichelsdoerfer, K. A. Brown, C. A. Mirkin, *Soft Matter* **2014**, *10*, 5603.
[63] A. Y. Malkin, A. Arinstein, V. G. Kulichikhin, *Prog. Polym. Sci.* **2014**, *39*, 959.
[64] J. L. Hedrick, K. A. Brown, E. J. Kluender, M. D. Cabezas, P.-C. Chen, C. A. Mirkin, *ACS Nano* **2016**, *10*, 3144.
[65] P. Hou, R. Kumar, B. Oberleiter, R. Kohns, D. Enke, U. Beginn, H. Fuchs, M. Hirtz, M. Steinhart, *Adv. Funct. Mater.* **2020**, *30*, 2001531.
[66] H. W. Fox, E. F. Hare, W. A. Zisman, *J. Phys. Chem.* **1955**, *59*, 1097.
[67] N. Shingne, M. Geuss, B. Hartmann-Azanza, M. Steinhart, T. Thurn-Albrecht, *Polymer* **2013**, *54*, 2737.

